

This is the accepted manuscript made available via CHORUS. The article has been published as:

Spin gaps in the ordered states of
 $\text{La}_{\{2\}}\text{LiXO}_{\{6\}}$ ($X=\text{Ru},\text{Os}$) and their relation to the
distortion of the cubic double perovskite structure in
 $4d^{\{3\}}$ and $5d^{\{3\}}$ magnets

D. D. Maharaj, G. Sala, C. A. Marjerrison, M. B. Stone, J. E. Greedan, and B. D. Gaulin

Phys. Rev. B **98**, 104434 — Published 28 September 2018

DOI: [10.1103/PhysRevB.98.104434](https://doi.org/10.1103/PhysRevB.98.104434)

Spin gaps in the ordered states of La_2LiXO_6 ($X = \text{Ru}, \text{Os}$) and their relation to distortion of the cubic double perovskite structure in $4d^3$ and $5d^3$ magnets.

D. D. Maharaj,^{1,*} G. Sala,^{1,2} C. A. Marjerrison,¹ M. B. Stone,² J. E. Greedan,^{3,4} and B. D. Gaulin^{1,4,5}

¹*Department of Physics and Astronomy, McMaster University, Hamilton, ON L8S 4M1 Canada*

²*Neutron Scattering Division, Oak Ridge National Laboratory, Oak Ridge, Tennessee 37831, USA*

³*Department of Chemistry and Chemical Biology, McMaster University, ON, L8S 4M1, Canada*

⁴*Brockhouse Institute for Materials Research, McMaster University, Hamilton, ON L8S 4M1 Canada*

⁵*Canadian Institute for Advanced Research, 661 University Ave., Toronto, ON M5G 1M1 Canada*

(Dated: August 13, 2018)

Time-of-flight inelastic neutron scattering measurements have been carried out on polycrystalline samples of the $4d^3$ and $5d^3$ double perovskite antiferromagnets $\text{La}_2\text{LiRuO}_6$ and $\text{La}_2\text{LiOsO}_6$. These reveal the development of an inelastic spin gap in $\text{La}_2\text{LiRuO}_6$ and $\text{La}_2\text{LiOsO}_6$ of $\sim 1.8(8)$ meV and $6(1)$ meV, below their respective ordering temperatures, T_N , ~ 23.8 K and 30 K. The bandwidth of the spin excitations is shown to be $\sim 5.7(9)$ to $12(1)$ meV, respectively, at low temperatures. Spin gaps are surprising in such magnets as the t_{2g} levels of Ru^{5+} or Os^{5+} are expected to be half-filled, resulting in an anticipated orbital singlet for both materials. We compare these results in monoclinic double perovskites $\text{La}_2\text{LiRuO}_6$ and $\text{La}_2\text{LiOsO}_6$ with those in cubic Ba_2YRuO_6 and Ba_2YOsO_6 , as well as with those in other monoclinic $\text{La}_2\text{NaRuO}_6$, $\text{La}_2\text{NaOsO}_6$, and $\text{Sr}_2\text{ScOsO}_6$, and model the inelastic magnetic scattering with linear spin wave theory using minimal anisotropic exchange interactions. We discuss the possible role of the distortion of the face-centered cubic, double perovskite structure on the spin gap formation and geometric frustration in these materials, and show that T_N scales with the top of the spin wave band in all members of these families that display long range order.

PACS numbers: 75.25.j, 75.40.Gb, 75.70.Tj

I. INTRODUCTION

Double perovskite antiferromagnets display a diverse set of quantum magnetic ground states due to the confluence of geometrical frustration and strong spin-orbit coupling, two topical trends in contemporary condensed matter physics¹. Their low temperature phase behavior has been the subject of much recent study - both experimental and theoretical in nature²⁻¹⁵. Double perovskites are characterized by a chemical formula of the form $A_2BB'O_6$, where the B and B' ions reside on octahedral sites, and form two interpenetrating face-centered cubic (FCC) lattices, provided that the overall structure is cubic. This is schematically shown in Fig. 1 a). If only one of the B or B' sites is magnetic, such a sublattice forms a single magnetic FCC lattice and in this configuration the magnetic moments decorate a network of edge-sharing tetrahedra as seen in Fig. 1 b). This generates one of the canonical architectures supporting geometrical frustration in three dimensions¹⁶.

These materials are such a rich platform for the study of quantum magnetism as the double perovskite structure is very flexible, and many magnetic and non-magnetic ions can occupy the B and B' sublattices. The overall crystal symmetry can be lower than cubic¹⁷ and, independently, the B and B' sublattices can mix at some low ($\sim 5\%$) level. Monoclinic symmetries typically arise due to correlated rotations of BO_6 and $B'O_6$ octahedra, as is shown in Fig. 1 c). Both $B - B'$ site mixing and distortions to structures with symmetry lower than cubic are controlled by the charge and ionic size difference between

the B and B' ions within the $A_2BB'O_6$ structure¹⁷. In this regard, the study of families of double perovskite systems can enable systematic investigations of magnetic materials where the size of the moment, and its quantum nature, as well as the role of spin-orbit coupling, can be varied systematically within, or between, the many families of these materials. Strong spin-orbit coupling in $5d$ systems is already known to induce a Mott instability in $5d^5$ iridate compounds, leading to an effective total angular momentum $J_{eff} = \frac{1}{2}$ state, distinct from the $S = 1/2$ localized state of conventional Mott insulators¹⁸, and is hence a route to novel quantum states of matter at low temperatures.

The $\text{Ba}_2\text{YB}'\text{O}_6$ family of double perovskites illustrates well the diversity of magnetic ground states that can be realized when the magnetic B' ion is occupied by different $4d$ or $5d$ transition metal ions. This family has been of particular recent interest as its structure remains cubic to low temperatures, enabling the realization of the perfect frustrated FCC magnetic sublattice. The family is also well ordered chemically, with only low levels ($\sim 1\%$) of $B - B'$ site mixing observed¹⁹⁻²¹. Specific members of this family studied to date include Ba_2YMoO_6 ($4d^1$), which exhibits a gapped collective spin-singlet ground state at low temperatures², Ba_2YReO_6 ($4d^2$) which shows an anomalous spin glass state below $T \sim 35$ K⁶ and Ba_2YRuO_6 ($4d^3$) and Ba_2YOsO_6 ($5d^3$), which both form the same type I antiferromagnetic (AF) structure below $T_N \sim 36$ K and 69 K, respectively^{3,4}. The structural and thermodynamic properties of Ba_2YIrO_6 ($5d^4$) have also been studied and it has been found to

remain paramagnetic down to 0.4 K¹¹.

Here we consider the $4d^3$ and $5d^3$ double perovskites, $\text{La}_2\text{LiRuO}_6$ and $\text{La}_2\text{LiOsO}_6$, with weak monoclinic distortions, and compare these new inelastic neutron scattering (INS) results to those previously obtained on the cubic d^3 systems, Ba_2YRuO_6 and Ba_2YOsO_6 as well as the monoclinic d^3 systems $\text{Sr}_2\text{ScOsO}_6$ and $\text{La}_2\text{NaRuO}_6$. The degree of distortion away from a cubic double perovskite structure can be parametrized by the average of the bond angle $\angle B - O - B'$ in monoclinic systems and subsequently compared to the cubic case where $\angle B - O - B' = 180^\circ$. This figure-of-merit indicates that the Sr_2ScXO_6 ($X = \text{Ru}, \text{Os}$) family is least distorted; with greater distortion in the La_2LiXO_6 family while the La_2NaXO_6 family is most distorted.

Like Ba_2YRuO_6 and Ba_2YOsO_6 , $\text{La}_2\text{LiRuO}_6$ and $\text{La}_2\text{LiOsO}_6$ are expected to have the same half-filling of their t_{2g} levels and thus display the same orbital singlet. $\text{La}_2\text{LiRuO}_6$ and $\text{La}_2\text{LiOsO}_6$ are also expected to differ from each other, primarily, through the strength of the spin-orbit coupling displayed by $4d^3$ ions compared to $5d^3$ ions. Earlier INS measurements on cubic Ba_2YRuO_6 and Ba_2YOsO_6 revealed spin gaps within their ordered states of ~ 5 meV and 17 meV, respectively^{3,4} with the gap of the $5d^3$ system being ~ 3 times larger than that in the $4d^3$ system⁴. The ratio of these spin gaps were found to be equal to the ratio of the free ion spin-orbit coupling factors, λ , for Os^{5+} ($\lambda = 186$ meV²²) and Ru^{5+} ($\lambda = 55$ meV²²), making a compelling argument that spin-orbit coupling stabilizes the d^3 spin gaps.

We have carried out a series of inelastic neutron scattering measurements on $\text{La}_2\text{LiRuO}_6$ and $\text{La}_2\text{LiOsO}_6$ in polycrystalline form. The form of the inelastic magnetic scattering above and below their respective T_N is seen to be qualitatively similar to that observed in Ba_2YRuO_6 and Ba_2YOsO_6 , in that the spin gaps develop coincident with T_N , and again scale roughly in proportion to expectations from atomic spin-orbit coupling factors. We can quantitatively account for the ground state spin excitation spectra using classical linear spin wave theory and a minimal microscopic spin Hamiltonian involving near-neighbor anisotropic exchange. We see that we get a very good description of the spin excitation spectra from all four d^3 double perovskite materials, that is for the new inelastic scattering data from monoclinic $\text{La}_2\text{LiRuO}_6$ and $\text{La}_2\text{LiOsO}_6$, and from our earlier data on cubic Ba_2YRuO_6 and Ba_2YOsO_6 . This then allows us to make systematic comparisons between the microscopic spin Hamiltonian parameters so estimated in these systems, and to formulate an understanding of how the ordering temperatures, T_N , are related to each other and to their Hamiltonians.

II. EXPERIMENT DETAILS

Time-of-flight INS measurements were performed using the direct geometry chopper spectrometer SE-

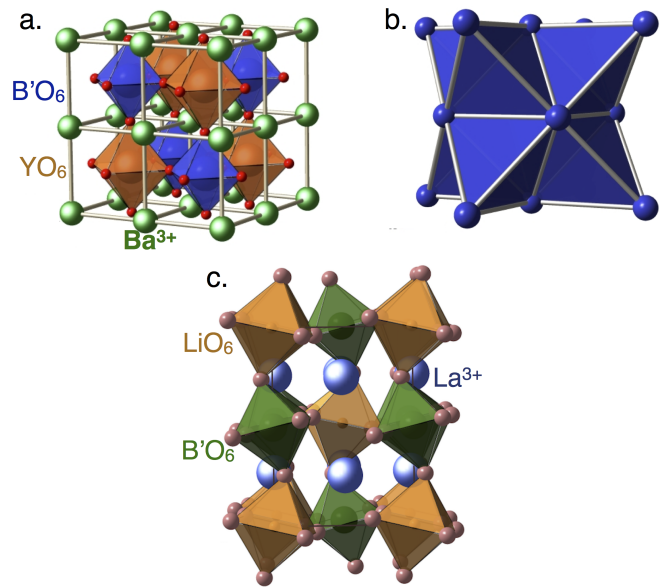


FIG. 1. The face-centered cubic (FCC) double perovskite structure exhibited by Ba_2YXO_6 ($X = \text{Ru}, \text{Os}$) and the lower symmetry structure of La_2LiXO_6 are shown in panels a) and c) respectively. In each structure the non-magnetic and magnetic B and B' ions co-ordinate with six oxygen atoms, forming a lattice of interpenetrating octahedra. The Ba^{3+} and La^{3+} atoms are distributed within this network. Panel b) shows the frustrated FCC network of edge-sharing tetrahedra of the B' site magnetic moments that are generated in the high symmetry Ba_2YXO_6 ($X = \text{Ru}, \text{Os}$) cubic structure.

QUOIA, BL-17, located at the Spallation Neutron Source (SNS) of Oak Ridge National Laboratory²³. Powder samples weighing 10 grams of each of $\text{La}_2\text{LiRuO}_6$ and $\text{La}_2\text{LiOsO}_6$ were packed in aluminium foil and placed in identical aluminium annular cans, ~ 3 cm in diameter. The two sample cans, as well as an empty sample can (used to obtain background measurements) were sealed in a glove box containing a He atmosphere to improve thermalization of the samples at low temperatures. The three cans were loaded on a three-sample carousel mounted to a closed-cycle refrigerator which produced a base temperature of 7 K.

Inelastic neutron scattering (INS) measurements were carried out on each sample using incident energies of $E_i = 40$ meV and 11 meV, which were both selected with chopper settings of $T_0 = 120$ Hz and $FC_2 = 60$ Hz. The elastic energy resolution associated with these INS measurements is $\sim 2\%$ of E_i , giving elastic energy resolutions of ~ 0.8 and 0.22 meV for $E_i = 40$ meV and 11 meV, respectively. These measurements were performed at a variety of temperatures above and below the respective Néel temperatures of $\text{La}_2\text{LiOsO}_6$ ($T_N = 30$ K) and $\text{La}_2\text{LiRuO}_6$ ($T_N = 23.8$ K). The data sets were reduced using Mantid²⁴ and analyzed using neutron scattering software DAVE²⁵.

III. NEUTRON SCATTERING RESULTS AND CALCULATIONS

A. Experiment Results and Analysis

Representative plots of the neutron scattering intensity as a function of energy transfer, $\hbar\omega$, and wavevector transfer, $|Q|$, appropriate to the powder samples of $\text{La}_2\text{LiRuO}_6$ and $\text{La}_2\text{LiOsO}_6$ are shown in Fig. 2 and 3, respectively, for several temperatures near and below T_N . Figure 2 shows data taken on $\text{La}_2\text{LiRuO}_6$ using $E_i = 11$ meV incident neutrons, while Fig. 3 shows data taken on $\text{La}_2\text{LiOsO}_6$ using $E_i = 40$ meV incident neutrons. In both cases an empty sample cell data set has been subtracted as a background. For both materials it is clear that a spin gap begins to develop near T_N , where $T_N = 23.8$ K for $\text{La}_2\text{LiRuO}_6$ and $T_N = 30$ K for $\text{La}_2\text{LiOsO}_6$. The spin gaps are well developed by $\frac{2}{3} \times T_N$ and fully formed by our base temperature of $T = 7$ K. The intensity scale for Figs. 2 and 3 is chosen to highlight the relatively weak inelastic scattering. The much stronger elastic scattering saturates the scale in both figures, but clear Bragg peaks are observed to develop below T_N at the 100 and 110 Bragg positions, near 0.8 \AA^{-1} and 1.15 \AA^{-1} , as reported in a separate account of the magnetic elastic scattering and structure⁵. For convenience, we employ the pseudo-cubic reciprocal lattice vector notations here and in the remainder of the paper.

Detailed cuts through the two dimensional data sets in the $\hbar\omega - |Q|$ maps of Figs. 2 and 3, are shown in Figs. 4 and 5, for $\text{La}_2\text{LiRuO}_6$ and $\text{La}_2\text{LiOsO}_6$, respectively. These cuts are taken by integrating around the 100 and 110 positions in $|Q|$; $0.6 < |Q| < 1.2 \text{ \AA}^{-1}$ for $\text{La}_2\text{LiRuO}_6$ with $E_i = 11$ meV neutrons in Fig. 4, and $0.6 < |Q| < 1.4 \text{ \AA}^{-1}$ for $\text{La}_2\text{LiOsO}_6$ with $E_i = 40$ meV neutrons in Fig. 5. At our base temperature of $T = 7$ K, we clearly identify a spin gap of $1.8(8)$ meV for $\text{La}_2\text{LiRuO}_6$ and $6(1)$ meV for $\text{La}_2\text{LiOsO}_6$. In both cases the spectral weight of the gapped magnetic scattering rises sharply from zero near the spin gap energy, and extends out with an energy-bandwidth of ~ 5.9 meV for $\text{La}_2\text{LiRuO}_6$ and ~ 12 meV for $\text{La}_2\text{LiOsO}_6$. The inelastic magnetic spectral weight in $\text{La}_2\text{LiRuO}_6$ appears to be bimodal, with the higher energy peak just below ~ 5 meV, as can be seen in the low temperature data in Fig. 4. For $\text{La}_2\text{LiOsO}_6$ in Fig. 5, one observes an extended high energy tail to the magnetic spectral weight above the spin gap at low temperatures. This is similar phenomenology to that displayed by the cubic double perovskites Ba_2YRuO_6 and Ba_2YOsO_6 , where their low temperature magnetic spectral weight above their, larger, spin gaps, are a factor of 1.5 to 2 larger in bandwidth than those observed in $\text{La}_2\text{LiRuO}_6$ and $\text{La}_2\text{LiOsO}_6$.

Figures 4 and 5 show in detail how the spin gap collapses in $\text{La}_2\text{LiRuO}_6$ and $\text{La}_2\text{LiOsO}_6$ and how the magnetic spectral weight fills in at low energies as the temperature moves towards and beyond their respective ordering temperatures. This is shown more quantitatively

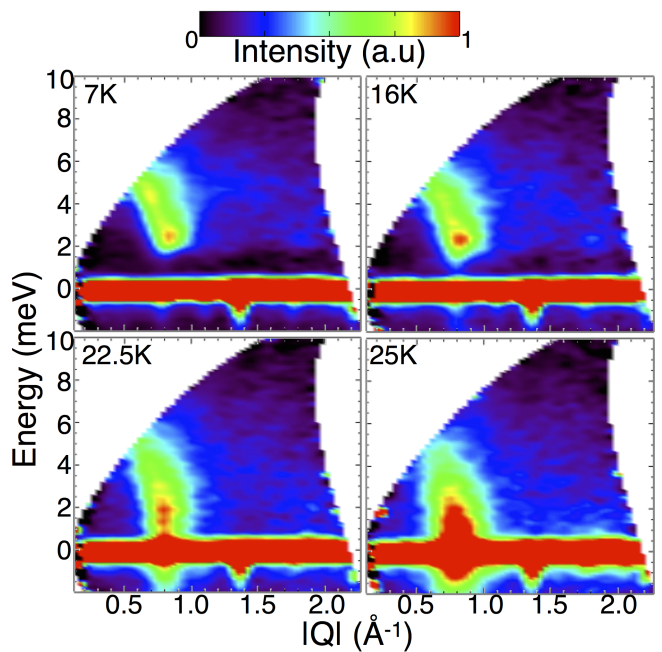


FIG. 2. Contour plots showing the inelastic neutron scattering intensity as a function of energy transfer, $\hbar\omega$ and wavevector transfer, $|Q|$, for $\text{La}_2\text{LiRuO}_6$ using $E_i = 11$ meV neutrons. Above $T_N = 23.8$ K there is an excess of quasi-elastic magnetic spectral weight centered near the (100) magnetic Bragg position at $|Q| = 0.8 \text{ \AA}^{-1}$. Below T_N , a spin gap develops and is fully formed by $T = 7$ K. An empty sample cell data set at $T = 7$ K has been subtracted from all displayed data sets.

in Figs. 6 and 7, where the temperature dependence of an integration of both the inelastic scattering, $S(|Q|, \omega)$, for energies above the spin gap, and the dynamic susceptibility, χ'' , for energies below the spin gap, is shown as a function of temperature for $\text{La}_2\text{LiRuO}_6$ and $\text{La}_2\text{LiOsO}_6$.

χ'' is related to the measured inelastic neutron scattered intensity by,

$$\Delta S(|Q|, \omega) = \frac{\chi''(|Q|, \hbar\omega)}{1 - e^{-\hbar\omega/k_B T}}. \quad (1)$$

Consideration of χ'' allows the temperature dependence from detailed balance, contained in the Bose factor, $1 - e^{-\hbar\omega/k_B T}$, to be removed, so that attention can focus on the physics of the system in question. However this analysis depends on a good understanding of the background. Assuming that there is no inelastic scattering at energies well below the spin gap at low temperatures, we can use a low temperature data set as the background, $T = 7$ K, and isolate χ'' as a function of temperature. The temperature dependence of this low energy χ'' is shown in Fig. 6 a) and Fig. 7 a) for $\text{La}_2\text{LiRuO}_6$ and $\text{La}_2\text{LiOsO}_6$, respectively. At energies above the spin gap, the inelastic magnetic scattering is never zero, and we look instead at the detailed temperature dependence of $S(|Q|, \omega)$ for $\text{La}_2\text{LiRuO}_6$ and $\text{La}_2\text{LiOsO}_6$ in Fig. 6 b) and

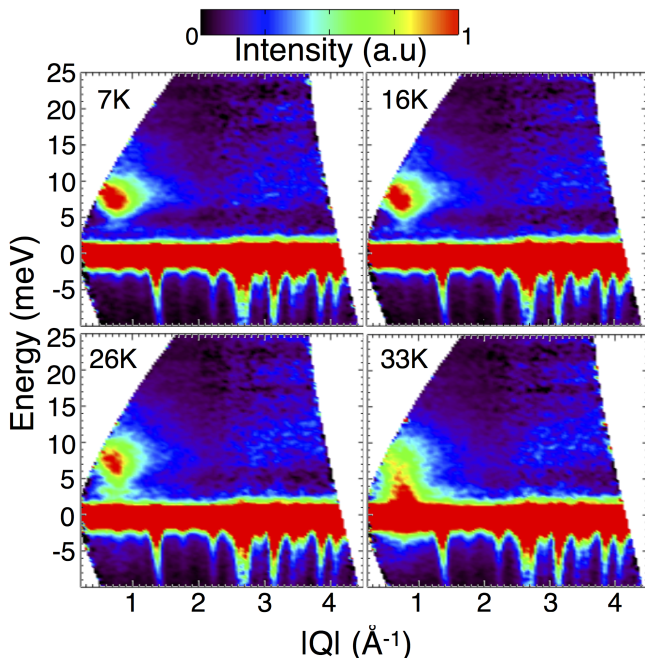


FIG. 3. Contour plots showing the inelastic neutron scattering intensity as a function of energy transfer, $\hbar\omega$ and wavevector transfer, $|Q|$, are shown above for $\text{La}_2\text{LiOsO}_6$ using the $E_i = 40$ meV neutron data set. Above $T_N = 30$ K there is an excess of quasi-elastic magnetic spectral weight centered near the magnetic (100) Bragg position $|Q| = 0.8 \text{ \AA}^{-1}$. Below T_N , a spin gap develops and is fully formed by $T = 7$ K. An empty sample cell data set at $T = 7$ K has been subtracted from all displayed data sets.

7 b), respectively.

Examination of Figs. 6 and 7 shows that T_N occurs at the inflection points of either the growth of χ'' below the spin gap, or the fall of $S(|Q|, \omega)$ above the spin gap, indicating that the formation of the spin gap is central to the magnetic phase transitions. For both $\text{La}_2\text{LiRuO}_6$ and $\text{La}_2\text{LiOsO}_6$ materials χ'' peaks at temperatures $\sim 10 - 20\%$ above T_N , and then slowly decreases as temperature increases towards their respective Curie-Weiss temperatures, ~ -204 K and -154 K, respectively.

The $|Q|$ dependence of χ'' at low energies within the spin gap is shown for $\text{La}_2\text{LiRuO}_6$ and $\text{La}_2\text{LiOsO}_6$ in Fig. 8. The energy integrations are performed over different ranges for $\text{La}_2\text{LiRuO}_6$ and $\text{La}_2\text{LiOsO}_6$ as the sizes of the spin gaps differ by a factor of ~ 3.3 . The $\text{La}_2\text{LiRuO}_6$ data employs an energy integration from $0.9 \text{ meV} < E < 1.4$ meV and Fig. 8 a) shows this $|Q|$ dependence as a function of temperature, for temperatures below and above $T_N = 23.8$ K. A very similar analysis is performed for $\text{La}_2\text{LiOsO}_6$ and the resulting $|Q|$ dependence of its low energy χ'' is shown in Fig. 8 b) for temperatures below and above its $T_N = 30$ K. In this case the energy is integrated over a larger range, from $0.9 \text{ meV} < E < 4.0$ meV.

The trends in the $|Q|$ dependence of low energy χ'' as

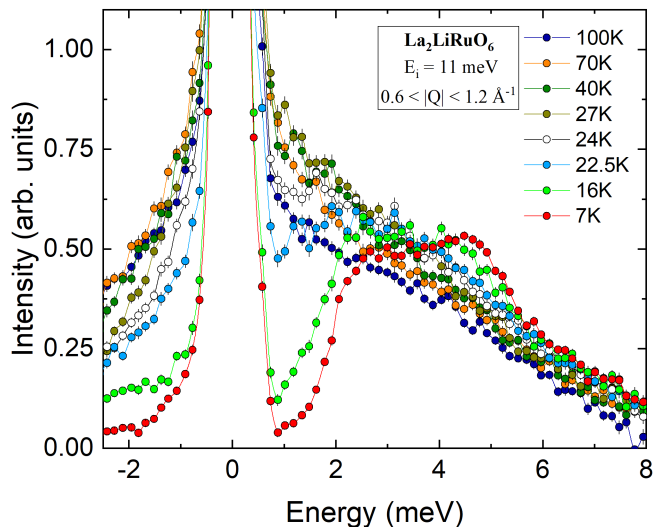


FIG. 4. $|Q|$ integrated ($|Q| = [0.6, 1.2] \text{ \AA}^{-1}$) cuts of the inelastic neutron scattering data shown in Fig. 2, showing the ~ 1.8 meV spin gap in $\text{La}_2\text{LiRuO}_6$. Above $T_N = 23.8$ K, quasi-elastic magnetic spectral weight is observed. At low temperatures, by $T = 7$ K, it is suppressed at energies low compared with the spin gap, and spectral weight shifts to higher energies where it is evident in a bimodal distribution of spin excitations with a total energy-bandwidth of ~ 5.7 meV.

a function of temperature are similar for the two materials. The $|Q|$ values appropriate to the (100) and (110) ordering wavevectors are denoted with vertical red fiducials in both panels of Fig. 8. One can see that χ'' ($|Q|, \hbar\omega < \Delta$) is centered primarily on the (100) ordering wavevector, and this peak rises in intensity as the temperature approaches T_N . The $|Q|$ dependence of χ'' ($|Q|, \hbar\omega < \Delta$) for $\text{La}_2\text{LiOsO}_6$ is, however, clearly broader than that of $\text{La}_2\text{LiRuO}_6$. This is likely a reflection of the different $(1/2 \ 1/2 \ 0)$ magnetic ordering wavevector that $\text{La}_2\text{LiOsO}_6$ displays, compared with the (100) type I AF ordering that $\text{La}_2\text{LiRuO}_6$ displays. The relative structure factor for the (110) magnetic Bragg intensity, compared with the (100) magnetic Bragg intensity, is stronger for the $(1/2 \ 1/2 \ 0)$ structure displayed by $\text{La}_2\text{LiOsO}_6$ than for the (100) structure displayed by $\text{La}_2\text{LiRuO}_6$. A natural explanation for the increased breadth in $|Q|$ for $\text{La}_2\text{LiOsO}_6$, is that the dynamic spectral weight is also relatively stronger at (110) and this extends the $|Q|$ dependence in χ'' from (100) to (110), therefore out to larger $|Q|$ s. As will be discussed below in the context of linear spin wave theory applied to these systems, the observed magnetic scattering in both systems falls off anomalously quickly with $|Q|$, likely related to co-valency of the 4 and 5d electrons, which implies a magnetic form factor corresponding to more extended d electron wavefunctions. This effect also tends to concentrate the inelastic scattering shown in Fig. 8 to smaller $|Q|$ than would otherwise be the case.

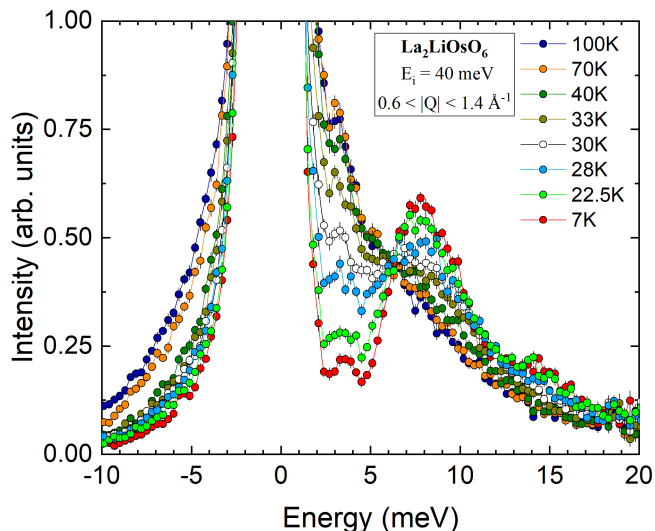


FIG. 5. $|Q|$ integrated ($|Q| = [0.6, 1.4] \text{ \AA}^{-1}$) cuts showing the ~ 6 meV spin gap in $\text{La}_2\text{LiOsO}_6$ at low temperatures. Above $T_N = 30$ K, quasi-elastic magnetic spectral weight is observed. Again the low energy scattering is suppressed below the spin gap below T_N . At $T = 7$ K a well developed spin gap is evident with spectral weight transferred to energies above the gap. The total energy-bandwidth of the spin excitations is ~ 12 meV.

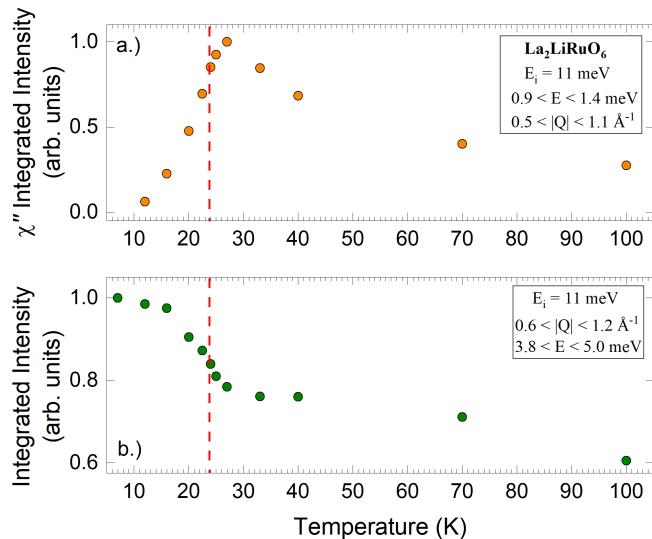


FIG. 6. The temperature dependence of χ'' for $\text{La}_2\text{LiRuO}_6$ is shown in panel a) where the integration of the intensity was performed in the range $|Q| = [0.5, 1.1] \text{ \AA}^{-1}$ and $E = [0.9, 1.4] \text{ meV} < \Delta$. Data taken at $T = 7$ K has been used as a background. This is derived from integrals of the data presented in Fig. 2. A complementary plot of the scattered intensity obtained from integrating $|Q| = [0.6, 1.2] \text{ \AA}^{-1}$ and $E = [3.8, 4.9] \text{ meV} > \Delta$ is shown in b). T_N is shown as the vertical dashed line in both panels.

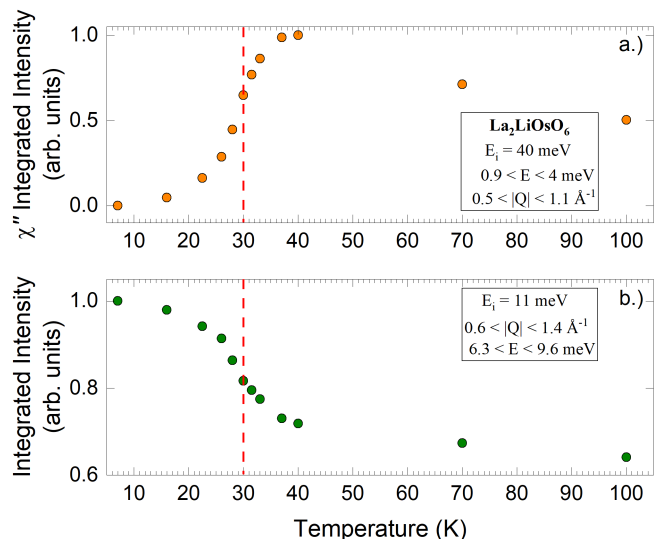


FIG. 7. The temperature dependence of χ'' for $\text{La}_2\text{LiOsO}_6$ is shown in a) where the integration of the intensity was performed in the range $|Q| = [0.5, 1.1] \text{ \AA}^{-1}$ and $E = [0.9, 4] \text{ meV} < \Delta$. Data taken at $T = 7$ K has been used as a background. This is derived from integrals of the data presented in Fig. 3. A complementary plot of the scattered intensity obtained by integrating $|Q| = [0.6, 1.4] \text{ \AA}^{-1}$ and $E = [6.3, 9.6] \text{ meV} > \Delta$ is shown in b). T_N is shown as the vertical dashed line in both panels.

B. Linear Spin Wave Theory Calculations

Linear spin wave theory calculations were carried out in order to estimate the microscopic spin Hamiltonian for the double perovskite systems $\text{La}_2\text{LiRuO}_6$, $\text{La}_2\text{LiOsO}_6$, Ba_2YRuO_6 and Ba_2YOsO_6 . The calculations were performed using the SpinW software package,²⁶ and these were benchmarked against the ground state ($T = 7$ K) inelastic neutron scattering data for $\text{La}_2\text{LiRuO}_6$ at $T = 7$ K in Fig. 2, for $\text{La}_2\text{LiOsO}_6$ at $T = 7$ K in Fig. 3, and using the corresponding data for Ba_2YRuO_6 , Ba_2YOsO_6 and $\text{La}_2\text{NaRuO}_6$, taken from previous studies performed by Carlo *et al.*³, Kermarrec *et al.*⁴ and Aczel *et al.*⁸, respectively.

The linear spin wave theory employed a minimal model for an anisotropic exchange Hamiltonian, which reproduces the type I AF ordered state displayed by $\text{La}_2\text{LiRuO}_6$, Ba_2YRuO_6 , and Ba_2YOsO_6 at low temperatures, and which also produces a gap in the low energy magnetic inelastic spectrum.

$$\mathcal{H} = -\left(J_1 \sum_{NN} \mathbf{S}_i \mathbf{S}_j + K_1 \sum_{NN} S_{i,x} S_{j,x} \right), \quad (2)$$

where the J_1 term represents an isotropic near-neighbor exchange interaction, related to the bandwidth of the spin excitations. The K_1 term generates the spin gap in these systems and an additional coupling of a particular component of spin, hence anisotropic exchange. J_1 and

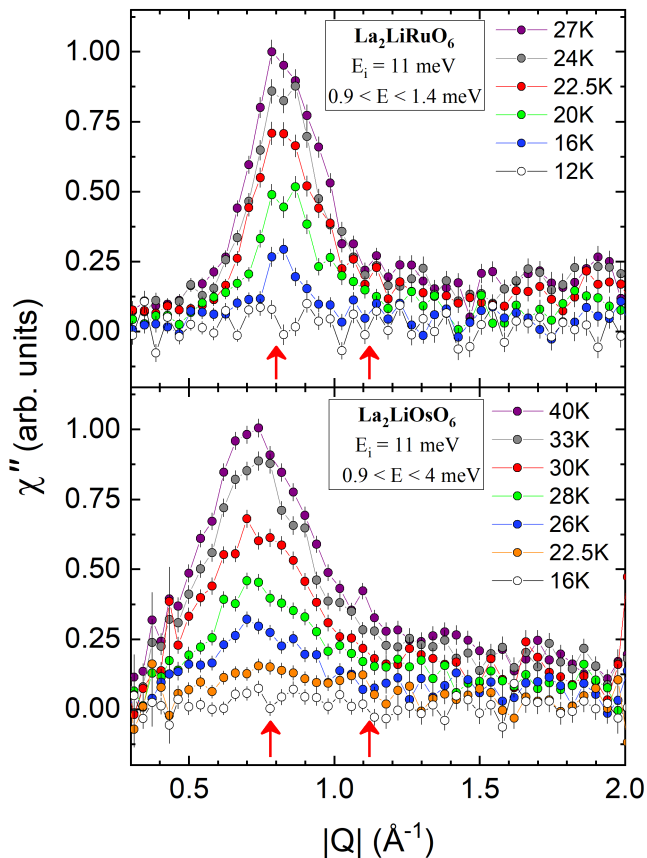


FIG. 8. a) The temperature dependence of χ'' for $\text{La}_2\text{LiRuO}_6$ is shown where integrations were performed with $|Q| = [0.5, 1.1] \text{ \AA}^{-1}$ and $E = [0.9, 1.4] \text{ meV} < \Delta$. Data taken at $T = 7 \text{ K}$ has been used as a background. This shows the $|Q|$ dependence of χ'' ($|Q|, E < \Delta$) and how it evolves as a function of temperature for temperatures below and just above T_N . b) The temperature dependence of low energy cuts of χ'' taken in the range $E = [0.9, 4] \text{ meV}$ for $\text{La}_2\text{LiOsO}_6$ are shown. This shows the $|Q|$ dependence of χ'' ($|Q|, E < \Delta$) and how it evolves as a function of temperature for temperatures below and just above T_N . In both panels, the red fiducial arrows indicate the positions of the (100) and (110) magnetic Bragg positions.

K_1 are defined such that positive values are ferromagnetic and negative values are antiferromagnetic. Near-neighbor anisotropic exchange interactions were previously identified as the likely cause for the spin gap observed in these d^3 systems^{4,10}, and a similar spin wave theory analysis was carried out by Taylor *et al*¹⁰ to model the spin excitation spectrum of the related monoclinic d^3 double perovskite, $\text{Sr}_2\text{ScOsO}_6$. The spin wave theory calculations were performed equivalently for both the cubic and monoclinic systems despite the slight distortion in the monoclinic systems, $\text{La}_2\text{LiOsO}_6$ and $\text{La}_2\text{LiRuO}_6$. These distortions are relatively weak and their inelastic neutron scattering spectra are remarkably similar to their cubic counterparts. The Os^{5+} magnetic form factor, obtained from work of Kobayashi *et al*²⁷, was employed in

our spin wave theory calculations. To our knowledge, the magnetic form factor for Ru^{5+} is not reported in the literature and as such, the Os^{5+} form factor was also used in the spin wave calculations for the Ru^{5+} systems³¹

The spectra obtained from calculations using equation 2 are shown in fig. 9 and the resulting fit parameters are presented in table I. The parameters provide good phenomenological descriptions of the observed spectra at low temperatures. The primary difference between the observed spectra and calculated spectra is that the intensity of the magnetic excitations drops off more rapidly as a function of $|Q|$ in the former case. This can be explained in terms of metal-ligand covalency effects between the d orbitals of the B' ions and the p orbitals of the neighboring O^{2-} ions^{4,8,10,28}. Thus the magnetic form factor for both Os^{5+} and Ru^{5+} should reflect more extended d electron wavefunctions, and thus drop off more sharply with $|Q|$.

The spin wave theory calculations were carried out, adjusting the two parameters in the spin Hamiltonian, J_1 and K_1 , using the inelastic neutron scattering for $\text{La}_2\text{LiRuO}_6$, $\text{La}_2\text{LiOsO}_6$, Ba_2YRuO_6 and Ba_2YOsO_6 as benchmarks, until a good description of the data was achieved. For comparison, literature data for $\text{La}_2\text{NaRuO}_6$ was also fit in this manner. Our best efforts resulted in the comparison between theory and experiment shown in Fig. 9. The resulting “best fit” parameters for J_1 and K_1 are shown both in the appropriate panels of Fig. 9 and are listed in Table 1 for all five double perovskites, as well as for $\text{Sr}_2\text{ScOsO}_6$, using the literature results from Taylor *et al*¹⁰. Comparing now between the $\text{Ba}_2\text{YRu/OsO}_6$ and $\text{La}_2\text{LiRu/OsO}_6$ families, it is clear that all the energy scales are higher in cubic $\text{Ba}_2\text{YRu/OsO}_6$ compared with $\text{La}_2\text{LiRu/OsO}_6$, consistent with the θ_{CW} values being higher in the cubic $\text{Ba}_2\text{YRu/OsO}_6$ family. Looking across the J_1 and K_1 parameters for the six double perovskites listed in Table I, we see that the anisotropic exchange values, K_1 are relatively consistent, $\sim -0.5 \text{ meV}$ for the ruthenates, and from -1.5 meV to -4 meV for the osmates. There is greater variation in the isotropic exchange parameter, J_1 , ranging from -0.3 meV for $\text{La}_2\text{NaRuO}_6$ which displays an incommensurate magnetic structure to -4.4 meV for $\text{Sr}_2\text{ScOsO}_6$ which displays the highest temperature phase transition, $T_N = 92 \text{ K}$, to a type I AF structure. Where the comparison can be made, in the $\text{Ba}_2\text{YRu/OsO}_6$ and $\text{La}_2\text{LiRu/OsO}_6$ families, the anisotropic near-neighbor exchange, K_1 , is much stronger in the osmate member of each family relative to the ruthenate member. This latter effect is responsible for the much higher spin gaps in the osmate members of the families compared to the ruthenates, and is consistent with spin-orbit coupling being ~ 3.2 times stronger in $5d^3 \text{ Os}^{5+}$ compared to $4d^3 \text{ Ru}^{5+}$ configurations.

The inelastic neutron scattering spectra can also be effectively reproduced using a spin Hamiltonian with isotropic near-neighbor exchange and single-ion anisotropy, as

System	J_1 (meV)	K_1 (meV)	D (meV)	$\frac{K_1}{J_1}$	$\frac{ D }{J_1}$
Ba ₂ YRuO ₆	-3.4	-0.65	1.3	0.2	0.4
Ba ₂ YOsO ₆	-1.7	-4.0	8.0	2.4	4.7
La ₂ LiRuO ₆	-1.1	-0.4	0.8	0.4	0.7
La ₂ LiOsO ₆	-0.9	-1.5	2.9	1.7	3.2
Sr ₂ ScOsO ₆	-4.4	-3.8	7.5	0.9	1.7
La ₂ NaRuO ₆	-0.3	-0.5	1.0	1.7	3.3

TABLE I. Microscopic exchange parameters relevant to each double perovskite system resulting from SpinW fits to the experimental spectra are shown. J_1 , K_1 and D represent isotropic nearest neighbor exchange, anisotropic nearest neighbor exchange and single-ion Ising-like anisotropy, respectively.

$$\mathcal{H} = -\left(J_1 \sum_{NN} \mathbf{S}_i \mathbf{S}_j + D \sum_i S_{i,x}^2\right), \quad (3)$$

The quality of the comparison between experiment and theory using this spin Hamiltonian is very similar to that using anisotropic exchange with Eq. 2, and hence this comparison is not reproduced here. The best fits to the inelastic spectra for La₂LiRuO₆, La₂LiOsO₆, Ba₂YRuO₆ and Ba₂YOsO₆, as well as Sr₂ScOsO₆ and La₂NaRuO₆, are listed in Table 1, where the same J_1 value is relevant to best fits with either single-ion anisotropy (Eq. 2) or anisotropic exchange (Eq. 1).

IV. DISCUSSION

The gapped magnetic excitation spectrum in the weakly monoclinic, double perovskite family La₂LiRuO₆ and La₂LiOsO₆ bears a striking resemblance to that observed in their corresponding cubic counterparts, Ba₂YRuO₆ and Ba₂YOsO₆, despite the fact that La₂LiRuO₆, Ba₂YRuO₆, and Ba₂YOsO₆ share a common magnetic structure below their respective ordering temperatures (T_N), while La₂LiOsO₆ displays a different AF structure⁵. It is therefore useful to make a quantitative comparison between the figures-of-merit for the magnetic properties and energy scales in these two families of double perovskites. This is what is shown in table II. We shall also discuss these trends in light of the microscopic spin Hamiltonians we have determined using spin wave theory and shown in table I.

Table II shows the measured T_N , ordered moment size, Curie-Weiss constants (θ_{CW}), spin wave bandwidths, and spin gaps for the cubic double perovskite family Ba₂YXO₆, and for the monoclinic double perovskite families La₂LiXO₆ and La₂NaXO₆, where X = Ru and Os. The ratio of the observed spin gaps within a particular Ru⁵⁺ and Os⁵⁺ family is also listed where possible, and, as previously discussed, it is as expected from atomic spin-orbit coupling, ~ 3.4 .

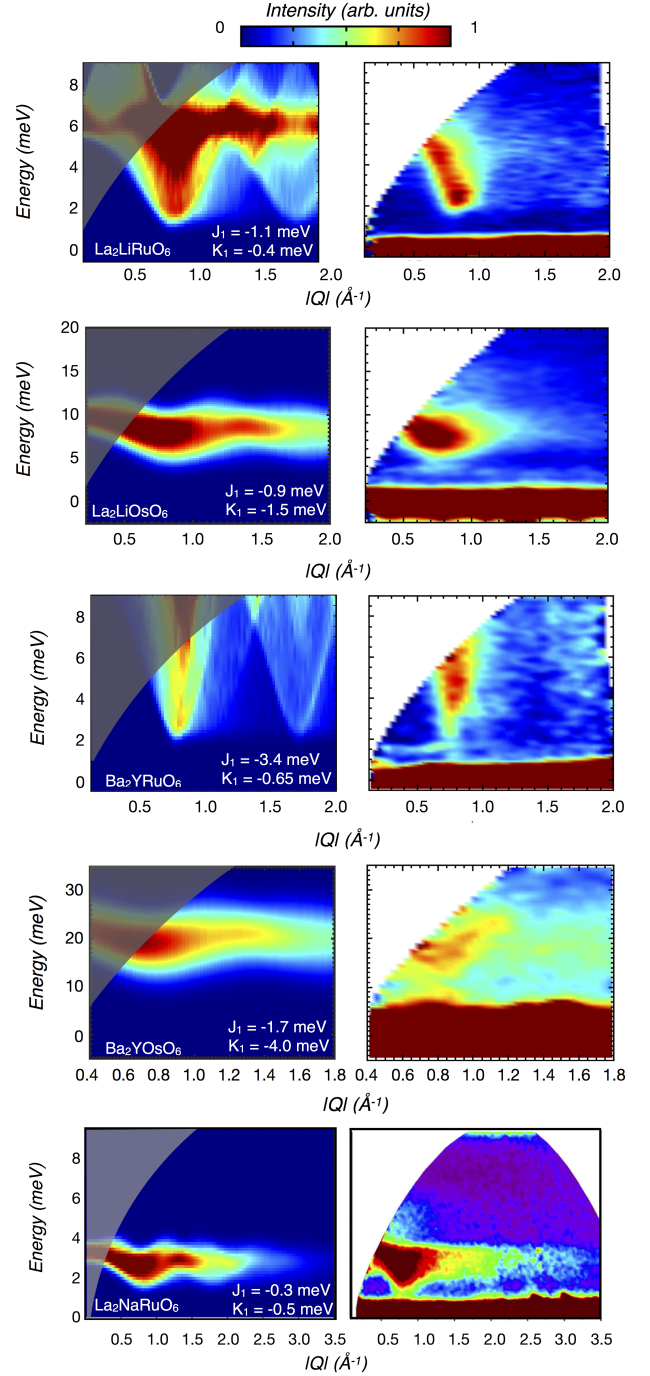


FIG. 9. The calculated spin wave spectra, performed with SpinW for the double perovskites, La₂LiRuO₆, La₂LiOsO₆, Ba₂YRuO₆, Ba₂YOsO₆, and La₂NaRuO₆ are presented in the left panels and the corresponding experimentally obtained INS spectra obtained at base temperatures are provided on the right. All experimental data sets are background subtracted. Appropriate Gaussian broadening of the calculated spin wave spectra was applied to each case, in order to account for experimental resolution.

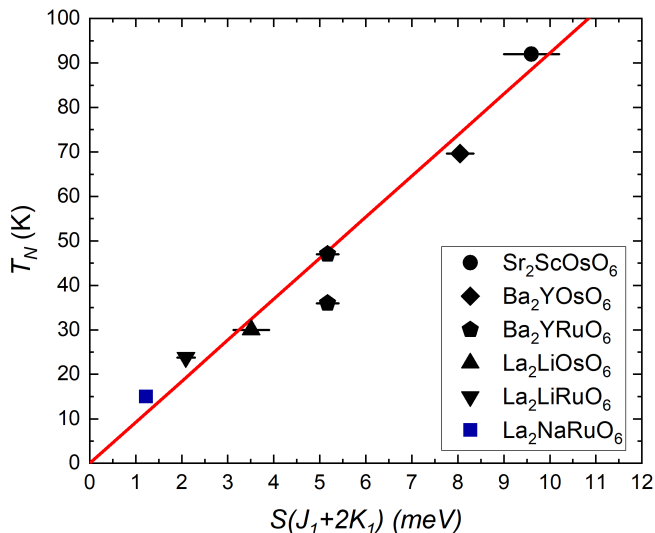


FIG. 10. The correlation between $S(J_1 + 2K_1)$ versus ordering temperature, T_N is shown for $\text{La}_2\text{LiRuO}_6$, $\text{La}_2\text{LiOsO}_6$, Ba_2YRuO_6 , Ba_2YOsO_6 , $\text{Sr}_2\text{ScOsO}_6$ and $\text{La}_2\text{NaRuO}_6$. The straight line is a fit to the data, constrained to go through the origin. Both transition temperatures reported by Carlo *et al*³ for Ba_2YRuO_6 are included in this plot, and the higher of the two temperatures T^* is employed in the fit.^a Please note that i.) the error bars associated with $S(J_1 + 2K_1)$ are due to S and as such, we expect this to be a lower limit on the estimate of the error in this quantity. ii.) the data point corresponding to $\text{La}_2\text{NaRuO}_6$ is highlighted in blue to emphasize that a $k = (0,0,0)$ type I AF magnetic structure was utilized for simplicity in the SpinW calculation. In actuality, the material exhibits an unusual incommensurate magnetic structure as reported in original work by Aczel *et al*⁸.

^a The fit is better using $T^* \sim 47$ K rather than $T_N = 36$ K, although both support the trend.

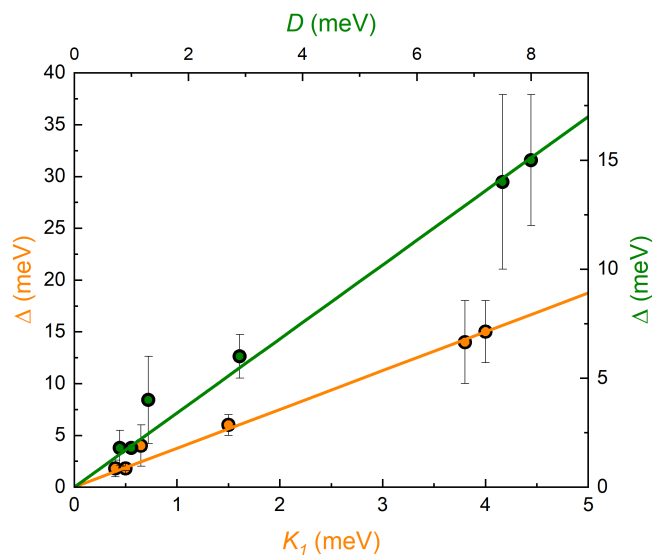


FIG. 11. The variation of the measured spin gap, Δ , with the anisotropic exchange parameter K_1 (in orange) and single-ion anisotropy D (in green) which are responsible for generating spin gaps within the model Hamiltonians.

One can see that a consistent picture emerges for the energy scales of the monoclinic $\text{La}_2\text{LiRuO}_6$ and $\text{La}_2\text{LiOsO}_6$ family relative to those of the cubic Ba_2YXO_6 ($X = \text{Ru}$ or Os) family, wherein all energy scales in the monoclinic family are smaller than those corresponding to the cubic family by factors of between 2 and 3. Note here that the Curie-Weiss constants for the cubic double perovskites, Ba_2YRuO_6 and Ba_2YOsO_6 , are well above room temperature, and thus difficult to accurately determine, as the high temperature regime of validity of such an analysis is not easily accessible. Nonetheless, the conclusion remains that the θ_{CW} values for Ba_2YRuO_6 and Ba_2YOsO_6 are substantially larger than their monoclinic counterparts, $\text{La}_2\text{LiRuO}_6$ and $\text{La}_2\text{LiOsO}_6$.

For this comparison we also include results from related monoclinic double perovskite systems: $\text{La}_2\text{NaRuO}_6$ and $\text{La}_2\text{NaOsO}_6$, and also $\text{Sr}_2\text{ScRuO}_6$ and $\text{Sr}_2\text{ScOsO}_6$ which have all been recently studied^{7-10,29}. To characterize the degree of the distortion of these monoclinic structures in relation to undistorted FCC structures, e.g. those exhibited by Ba_2YOsO_6 and Ba_2YRuO_6 , we ascribe the average of the angle $\angle B - O - B'$. For FCC double perovskites, with a single oxygen site, the $B - O - B' = 180^\circ$. For monoclinic double perovskites however, $B - O - B' < 180^\circ$ and a smaller $\angle B - O - B'$, corresponds to more severe distortion from FCC. The energy scales of the $\text{La}_2\text{NaRuO}_6$ and $\text{La}_2\text{NaOsO}_6$ family, with relatively large distortion away from FCC, are all suppressed relative to the less distorted La_2LiXO_6 and Ba_2YXO_6 families; so much so that $\text{La}_2\text{NaOsO}_6$ does not order to temperatures as low as 7 K, while $\text{La}_2\text{NaRuO}_6$ orders into an unusual incommensurate structure below $T_N \sim 15$ K⁷. This incommensurate structure is unique among these d^3 systems, and has been attributed to the considerable tilting of the NaO_6 and Os/RuO_6 octahedra implied by the low $\angle B - O - B'$ values they display. This is argued to randomize the strength of near neighbor exchange interactions, such that they are, on average, weaker. This could also lead to competition between near-neighbor J_1 interactions and next near-neighbor, J_2 , interactions⁹ leading to incommensurate magnetic structures. $\text{Sr}_2\text{ScOsO}_6$ and $\text{Sr}_2\text{ScRuO}_6$ are interesting comparators as these structures are more weakly distorted than either of La_2LiXO_6 or La_2NaXO_6 , and they exhibit the highest T_N s and highest θ_{CW} of these three families of monoclinic double perovskites. In fact $\text{Sr}_2\text{ScOsO}_6$ exhibits $T_N = 92$ K, which is 1/3 higher than the $T_N = 69$ K exhibited by FCC Ba_2YOsO_6 and a spin gap roughly the same as Ba_2YOsO_6 , $\Delta = 14(4)$ meV.

This comparison suggests that the tilting of the BO_6 and $\text{B}'\text{O}_6$ octahedra systematically weakens the interaction energy scales in these families of double perovskites, but it is not the only factor. Indeed first principles density-functional theory calculations show that for a series of compounds, $\text{Sr}_2\text{ScB}'\text{O}_6$ where $B' = (\text{Y}, \text{In}, \text{Sc})$, Sc is the strongest mediator of magnetic exchange interactions due to the overlap in energy between the Os-5d and

the Y/In/Sc- d states, even though the same magnetic ion and same magnetic ground state is involved¹². The relative strengths of Y^{3+} and Sc^{3+} in mediating exchange is also consistent with Sr_2YO_6 ordering at $T_N = 53$ K³⁰ while Sr_2ScOsO_6 orders at $T_N = 92$ K⁹, which in turn is larger than the $T_N = 69$ K of FCC Ba_2YO_6 ⁴.

The wide variation in T_N observed in the d^3 systems is considered in Fig. 10, and an excellent linear relationship between T_N and $S(J_1 + 2K_1)$, going through the origin, is observed. This is consistent with the observation that T_N scales according to the top of the spin wave band in all these double perovskite magnets. Figure 11 demonstrates how K_1 generates the spin gap (as does single-ion anisotropy D). J_1 generates the spin wave bandwidth, while both the bandwidth and the spin gap scale as the moment size, S . Hybridization of the d electron orbitals is stronger for the $5d$ osmates compared to the $4d$ ruthenates, and this appears to result in a lower ordered moment, S , in the osmates compared to the ruthenates. K_1 is empirically observed to be twice as effective at increasing the gap as J_1 is to increasing the bandwidth. Both contribute equally to the energy of the top of the spin wave band, and this then gives the relation that T_N is expected to increase as $S(J_1 + 2K_1)$, as Fig. 10 illustrates.

Table II show that the frustration index f , defined as the ratio of θ_{CW} to T_N , is highest for the cubic double perovskites, ~ 10 , as expected. The high symmetry of the face centred cubic structure allows the most competition among equivalent interactions. This condition is expected to be relaxed somewhat as the symmetry is lowered to monoclinic. We see that the cubic double perovskites display frustration indices of ~ 10 , which is about 30 % greater than those displayed by the monoclinic double perovskites in this comparator group. A frustration index of 10 is large, comparable to those exhibited, for example, by the $4d^2$ pyrochlore antiferromagnets $Y_2Mo_2O_7$ and $Lu_2Mo_2O_7$, both of which exhibit frozen spin glass states at sufficiently low temperatures. However these f values are not as large as those found in quasi-two dimensional $3d^9$ Kagome antiferromagnets, such as Herbertsmithite, $ZnCu_3(OH)_6Cl_2$, where f exceeds 200.

V. CONCLUSIONS

To conclude, we have studied the inelastic magnetic scattering and corresponding spin gaps in the weakly monoclinic, double perovskite antiferromagnets La_2LiRuO_6 and La_2LiOsO_6 using time-of-flight inelastic neutron scattering techniques. We observe the spin gaps to collapse on passing through T_N . The spin gaps themselves, 1.8(8) meV for La_2LiRuO_6 and 6(1) meV for La_2LiOsO_6 , scale with the strength of the atomic spin-orbit coupling parameter, λ , appropriate for $4d^3$ Ru^{5+} and $5d^3$ Os^{5+} . Such a spin gap is naively unanticipated for a d^3 system due to the orbital singlet expected from half-filled t_{2g} levels. The magnetic spectral weight in

La_2LiRuO_6 and La_2LiOsO_6 below their respective T_N s is well described by linear spin wave theory, based on near-neighbor anisotropic exchange, as is the low temperature magnetic spectral weight in the cubic double perovskites Ba_2YRuO_6 and Ba_2YO_6 , which were previously measured.

A similar spin wave analysis was carried out earlier for Sr_2ScOsO_6 , and the T_N s for this family of 5 double perovskite antiferromagnets scales very well with $S(J_1 + 2K_1)$, which characterizes the energy of the top of the spin wave band in all of these materials. The magnitude of the spin wave gap is controlled by the near-neighbor anisotropic exchange strength, K_1 , and together these are strong evidence for the gapped spectrum arising due to anisotropic exchange, which itself is generated by spin-orbit coupling. We hope that these new measurements and their analysis in the context of spin dynamics in other d^3 double perovskites can guide a full understanding of the nature of their ordered states and counter-intuitive spin gaps.

VI. ACKNOWLEDGMENTS

Research at McMaster University was supported by NSERC of Canada. This work was supported in part by the National Science Foundation under Grant No. PHYS-1066293 and the hospitality of the Aspen Center for Physics. We also acknowledge the hospitality of the Telluride Science Research Center. We gratefully acknowledge useful conversations with A. Taylor, R. F. Fishman, and S. Calder. We are very grateful for the instrument and sample environment support provided during our inelastic neutron scattering measurements at SEQUOIA. The experiments which were performed at the Spallation Neutron Source at Oak Ridge National Laboratory was sponsored by the US Department of Energy, Office of the Basic Energy Sciences, Scientific User Facilities Division.

TABLE II. A summary of key properties of d^3 double perovskites considered in this comparison are shown in this table. Please note that a.) INS studies have not been performed on the Ru based compound, $\text{Sr}_2\text{ScRuO}_6$ and as such Δ_{Os}/Δ_{Ru} is not reported for this family of double perovskites b.) numerical values for T_N , μ , f and Δ are not quoted for $\text{La}_2\text{NaOsO}_6$ as it fails to develop long range order as determined in studies by Aczel *et al*^{7,8} c.) the values quoted for Δ in this table are the values which have been defined using the convention described earlier in Section III B and will not correspond to the reported in original work on these materials^{3,4,8,10} and d.) The bond angles $\angle B-O-B'$ were retrieved from published crystallographic studies outlined in the footnotes at the bottom of this table.

System	T_N (K)	μ	θ_{CW} (K)	Bandwidth (meV)	$\angle B-O-B'$ ($^\circ$)	f ($\equiv \theta_{CW} /T_N$)	Δ (meV)	Δ_{Os}/Δ_{Ru}	Ref.
Ba_2YRuO_6	36	$2.2(1)\mu_B$	-399(2)	11(2)	180	11	4(2)	3.8	[3]
Ba_2YOsO_6	69	$1.65(6)\mu_B$	-717(5)	16(3)	180	11	15(3)		[4]
$\text{La}_2\text{LiRuO}_6$	23.8	$2.2(2)\mu_B$	-185(5)	5.7(9)	155.1(4) ^a	9	1.8(8)	3.3	[5], this work
$\text{La}_2\text{LiOsO}_6$	30	$1.8(2)\mu_B$	-154(2)	12(1)	153.5(5) ^b	6	6(1)		[5], this work
$\text{La}_2\text{NaRuO}_6$	15(1)	$1.87(7)\mu_B$	-57(1)	2.0(3)	146.00(22) ^c	4	1.8(2)	-	[7,8]
$\text{La}_2\text{NaOsO}_6$	-	-	-74(1)	-	145.4(5) ^d	-	-	-	[7,8]
$\text{Sr}_2\text{ScRuO}_6$	60	$1.97(2)\mu_B$	-242	-	178.7(6)	4	-	-	[29]
$\text{Sr}_2\text{ScOsO}_6$	92(1)	$1.6(1)\mu_B$	-677	20(4)	165.5(6)	7.4	14(4)	-	[9,10]

^a P. D. Battle, C. P. Grey, M. Hervieu, C. Martin, C. A. Moore, and Y. Paik, J. Solid State Chem. **175**, pp. 20-26 (2003).

^b W. R. Gemmill, M. D. Smith, and H.-C. zur Loye, J Solid State Chem. **179**, pp 1750-1756 (2006).

^c W. R. Gemmill, M. D. Smith, and H.-C. zur Loye, J Solid State Chem. **177**, pp 3560-3567 (2004).

^d W. R. Gemmill, M. D. Smith, R. Prozorov, and H.-C. zur Loye, Inorg. Chem. **44**, pp 2639-2646 (2005).

* maharadd@mcmaster.ca

- ¹ W. Witczak-Krempa, G. Chen, Y. B. Kim, and L. Balents, *Annu. Rev. Condens. Matter Phys.* **5**, 1 (2014).
- ² J. P. Carlo, J. P. Clancy, T. Aharen, Z. Yamani, J. P. C. Ruff, J. J. Wagman, G. J. Van Gastel, H. M. L. Noad, G. E. Granroth, J. E. Greedan, H. A. Dabkowska, and B. D. Gaulin, *Phys. Rev. B* **84**, 100404 (2011).
- ³ J. P. Carlo, J. P. Clancy, K. Fritsch, C. A. Marjerrison, G. E. Granroth, J. E. Greedan, H. A. Dabkowska, and B. D. Gaulin, *Phys. Rev. B* **88**, 024418 (2013).
- ⁴ E. Kermarrec, C. A. Marjerrison, C. M. Thompson, D. D. Maharaj, K. Levin, S. Kroeker, G. E. Granroth, R. Flacau, Z. Yamani, J. E. Greedan, and B. D. Gaulin, *Phys. Rev. B* **91**, 075133 (2015).
- ⁵ C. M. Thompson, C. A. Marjerrison, A. Z. Sharma, C. R. Wiebe, D. D. Maharaj, G. Sala, R. Flacau, A. M. Hallas, Y. Cai, B. D. Gaulin, G. M. Luke, and J. E. Greedan, *Phys. Rev. B* **93**, 014431 (2016).
- ⁶ C. M. Thompson, J. P. Carlo, R. Flacau, T. Aharen, I. A. Leahy, J. R. Pollichiemi, T. J. S. Munsie, T. Medina, G. M. Luke, J. Munevar, S. Cheung, T. Goko, Y. J. Uemura, and J. E. Greedan, *J. Phys.: Condens. Matter* **26**, 306003 (2014).
- ⁷ A. A. Aczel, D. E. Bugaris, L. Li, J.-Q. Yan, C. de la Cruz, H. C. zur Loye, and S. E. Nagler, *Phys. Rev. B* **87**, 014435 (2013).
- ⁸ A.A. Aczel, P.J. Baker, D.E. Bugaris, J. Yeon, H. C. zur Loye, T. Guidi, and D.T. Adroja, *Phys. Rev. Lett.* **112**, 117603 (2014).
- ⁹ A. E. Taylor, R. Morrow, D. J. Singh, S. Calder, M. D. Lumsden, P. M. Woodward, and A. D. Christianson, *Phys. Rev. B* **91**, 100406 (2015).
- ¹⁰ A. E. Taylor, R. Morrow, R. S. Fishman, S. Calder, A. I. Kolesnikov, M. D. Lumsden, P. M. Woodward, and A. D. Christianson, *Phys. Rev. B* **93**, 220408 (2016).
- ¹¹ T. Dey, A. Maljuk, D. V. Efremov, O. Kataeva, S. Gass, C. G. F. Blum, F. Steckel, D. Gruner, T. Ritschel, A. U. B. Wolter, J. Geck, C. Hess, K. Koepernik, J. van den Brink, S. Wurmehl, and B. Büchner, *Phys. Rev. B* **93**, 014434 (2016).
- ¹² S. Kanungo, B. Yan, C. Felser, and M. Jansen, *Phys. Rev. B* **93**, 161116 (2016).
- ¹³ F.-Y. Li, Y.-D. Li, Y. Yu, A. Paramekanti, and G. Chen, *Phys. Rev. B* **95**, 085132 (2017).
- ¹⁴ G. Chen, R. Pereira, and L. Balents, *Phys. Rev. B* **82**, 174440 (2010).
- ¹⁵ G. Chen, and L. Balents, *Phys. Rev. B* **84**, 094420 (2011).
- ¹⁶ C. Lacroix, P. Mendels, and F. Mila, *Introduction to Frustrated Magnetism* (Springer-Verlag, Berlin Heidelberg, 2011).
- ¹⁷ M. T. Anderson, K. B. Greenwood, G. A. Taylor, and K. R. Poeppelmeier, *Prog. Solid State Chem.* **22**, pp. 197-223 (1993).
- ¹⁸ B. J. Kim, H. Ohsumi, T. Komesu, S. Sakai, T. Morita, H. Takagi, and T. Arima, *Science* **323**, 1167106 (2009).
- ¹⁹ T. Aharen, J. E. Greedan, F. Ning, T. Imai, V. K. Michaelis, S. Kroeker, H. Zhou, C. R. Wiebe, and L. M. D. Cranswick, *Phys. Rev. B* **80**, 134423 (2009).
- ²⁰ T. Aharen, J. E. Greedan, C. A. Bridges, A. A. Aczel, J. Rodriguez, G. MacDougall, G. M. Luke, T. Imai, V. K. Michaelis, S. Kroeker, H. Zhou, C. R. Wiebe, and L. M. D. Cranswick, *Phys. Rev. B* **81**, 224409 (2010).
- ²¹ T. Aharen, J. E. Greedan, C. A. Bridges, A. A. Aczel, J. Rodriguez, G. MacDougall, G. M. Luke, V. K. Michaelis, S. Kroeker, C. R. Wiebe, H. Zhou, and L. M. D. Cranswick, *Phys. Rev. B* **81**, 064436 (2010).
- ²² C.-G. Ma and M. G. Brik, *J. Lumin.* **145**, pp. 402-409 (2014).
- ²³ G. E. Granroth, A. I. Kolesnikov, T. E. Sherline, J. P. Clancy, K. A. Ross, J. P. Ruff, B. D. Gaulin, and S. E. Nagler, *J. Phys. Conf. Ser.* **251**, 12058 (2010).
- ²⁴ O. Arnold, J. C. Bilheux, J. M. Borreguero, A. Buts, S. I. Campbell, L. Chapon, M. Doucet, N. Draper, R. Ferraz Leal, M. A. Gigg, V. E. Lynch, A. Markvardsen, D. J. Mikkelsen, R. L. Mikkelsen, R. Miller, K. Palmen, P. Parker, G. Passos, T. G. Perring, P. F. Peterson, S. Ren, M. A. Reuter, A. T. Savici, J. W. Taylor, R. J. Taylor, R. Tolchenov, W. Zhou, and J. Zikovsky, *Nucl. Instr. Meth. Phys. Res. A* **764**, pp. 156-166 (2014).
- ²⁵ R. T. Azuahl, L. R. Kneller, Y. Qiu, P. L. W. Tregenna-Piggott, C. M. Brown, J. R. D. Copley, and R. M. Dimeo *J. Res. Natl. Inst. Stand. Technol.* **114**, 341 (2009).
- ²⁶ S. Tóth, and B. Lake, *J. Phys.: Condens. Matter* **27**, 166002 (2015).
- ²⁷ K. Kobayashi, T. Nagao, and M. Ito, *Acta Cryst. A.* **67**, pp. 473-480 (2011).
- ²⁸ E. Granado, J. W. Lynn, R. F. Jardim, and M. S. Torikachvili, *Phys. Rev. Lett.* **110**, 017202 (2013).
- ²⁹ P. Kayser, S. Injac, B. Ranjbar, B. J. Kennedy, M. Avdeev, and K. Yamaura, *Inorg. Chem.* **56**, pp. 9009-9018 (2017).
- ³⁰ A. K. Paul, A. Sarapulova, P. Adler, M. Reehuis, S. Kanungo, D. Mikhailova, W. Schnelle, Z. Hu, C. Kuo, V. Siruguri, S. Rayaprol, Y. Soo, B. Yan, C. Felser, L. H. Tjeng, and M. Jansen, *Z. Anorg. Allg. Chem.* **641**, pp. 197-205 (2015).
- ³¹ The $\langle j_0 \rangle$ parameters for $4d$ and $5d$ magnetic form factors corresponding to the same number of d electrons, e.g. W^+ and Mo^+ differ little, as do the form factors associated with Os^{4+} , Os^{5+} and Os^{6+} . We therefore consider the Os^{5+} form factor a good proxy for that of Ru^{5+} . Consideration of the weak $\langle j_2 \rangle$ contribution extends the form factor to higher $|Q|$, which is opposite to the effect of covalency between the $4/5d$ orbitals of the magnetic ion and $2p$ orbitals of the O^{2-} ion.